Research Article

Nanohybrids Near-Field Optical Microscopy: From Image Shift to Biosensor Application

Nayla El-Kork,[1,2,3] Paul Moretti,[1] Bernard Jacquier,[1] Feiran Lei,[4] and Mohammed Ismail[2,3,4]

[1]*Institut Lumière Matière (ILM), UMR5306 Université Lyon 1-CNRS, Université de Lyon, 69622 Villeurbanne Cedex, France*
[2]*Khalifa University of Science, Technology, and Research (KUSTAR), Sharjah Campus, P.O. Box 127788, Abu-Dhabi, UAE*
[3]*Khalifa Semiconductor Research Center, Khalifa University, Room 328, F Building, Abu Dhabi, UAE*
[4]*Department of Electrical and Computer Engineering, The Ohio State University, 2015 Neil Avenue, Columbus, OH 43210, USA*

Correspondence should be addressed to Nayla El-Kork; nayla.elkork@kustar.ac.ae

Near-Field Optical Microscopy is a valuable tool for the optical and topographic study of objects at a nanometric scale. Nanoparticles constitute important candidates for such type of investigations, as they bear an important weight for medical, biomedical, and biosensing applications. One, however, has to be careful as artifacts can be easily reproduced. In this study, we examined hybrid nanoparticles (or nanohybrids) in the near-field, while in solution and attached to gold nanoplots. We found out that they can be used for wavelength modulable near-field biosensors within conditions of artifact free imaging. In detail, we refer to the use of topographic/optical image shift and the imaging of Local Surface Plasmon hot spots to validate the genuineness of the obtained images. In summary, this study demonstrates a new way of using simple easily achievable comparative methods to prove the authenticity of near-field images and presents nanohybrid biosensors as an application.

1. Introduction

Scanning Near-Field Optical Microscope (SNOM) artifacts have been the cause of several debates, for microscopes with an auxiliary gap width regulation. Scientists have suspected the existence of severe artifacts in constant distance SNOM when they frequently found a one-to-one correspondence between optical and topographic images and their corresponding resolution. They concluded that the produced images represented the path of the probe rather than optical properties of the sample [1, 2]. This is because it is of little probability that two imaging processes that result from different physical origins have identical resolving power [3]. To overcome this problem, one can use constant height SNOM, as in this case the regulations system does not take into account the curvatures of the sample. Having this in mind, constant height SNOM is not designed within all SNOM systems. Also, one cannot deny the importance of the additional topographic information that constant distance SNOM can offer. Up to our knowledge, no specific verification method has been confirmed suitable for recognizing artifact free

optical SNOM images, without referral to constant height regulation.

We show in this paper how we can verify with a simple method the genuine nature of constant distance optical SNOM images. We will refer to the investigation of hybrid nanoparticles (called nanohybrids), designed for biosensing application through Local Surface Plasmon Resonance (LSPR) hot spots imaging.

This paper is organized into three parts: In Section 2.1, we will present near- and far-field spectroscopic characterisation of the nanohybrids. We then analyze the corresponding SNOM setup operating conditions. Finally, we present a verification procedure that would allow one to assert the validity of SNOM measurements without referring to constant height scans. In Section 2.2, we will show SNOM images of LSPR hot spots on gold nanoplots, in addition to corresponding Finite Element Method (FEM) simulations. Both will serve in Section 2.3 to demonstrate the possible use of the nanohybrids in a gold nanoplots biosensor and the veracity of the verification method, presented in Section 2.1 of the paper.

2. Results and Discussion

2.1. Nanohybrid Investigations

2.1.1. Experimental

(A) The Nanohybrids. Hybrid nanoparticles are a new class of organic/inorganic materials [4]. They can be single-phased or associated (core/shell) and functionalized on the surface with bonds linking the particle to molecular elements. We studied a nanohybrid that is chemically synthesized by Nano-H company [5]. It is composed of a gadolinium oxide core doped with Tb^{+3} and covered with a polysiloxane shell containing fluorescent molecules [6, 7]; its overall diameter is 20 nm. The gadolinium oxide core is usually known for its optical, magnetic, and therapeutic advantages; however, in our case, it will be only used as a support for the external shell. The role of the last is to chemically protect the nanoparticles from any agent in the external media and to hold an important modifiable quantity of complementary organic fluorophores (Fluorescein (FITC)), Rhodamine B (RBITC), and so forth. The nanohybrids are presented in a water solution at a concentration of 0.5 mg/L. Marked nanoparticles usually show emission spectra corresponding to their specific fluorophores. This property is essential for the function of the nanoparticles as biomarkers.

(B) Sample Preparation. Two different samples were prepared for nanohybrid characterisation:

> Sample 1 consists of a glass substrate on which a drop of the nanoparticles solution is left drying in air at room temperature, for few hours.

> Sample 2 is made of uniformly dispersed nanoparticles on a thin cover glass. It is prepared by spinning a drop of the nanoparticles solution on the substrate, at high frequency for few minutes. The dispersion of the nanoparticles essentially takes place in two different stages: First the spinning centrifugal force ejects an important amount of the solution from the substrate, leaving a thin uniform liquid film on its surface. Then as the solvent evaporates, the solute deposits on the support [8]. The spacing and the distribution of the nanoparticles depend on parameters such as the concentration of the original solution, the rotation frequency, the evaporation rate of the solvent, and the solvent/substrate contact angle [9, 10].

(C) Far-Field Measurements. We have done all our far-field measurements (absorption and emission) at room temperature. The setup used for acquiring emission spectra is shown in Figure 1(a): an argon laser (Laser Coherent Innova 300) directed toward the hybrid nanoparticles emits ($\lambda = 488$ nm) with a power of few milliwatts. A system of lenses leads the resulting fluorescence light toward a monochromator (Jobin-Yvon H25 monochromator), and a water cooled photomultiplier tube (C31034 Series Burle electron tube); finally, a lock-in amplifier system (EG&G Princeton Applied Research Model 5205) and a chopper are used to eliminate any background signal. A notch filter at $\lambda = 488$ nm (Kaiser Optical Systems Holographic Notch Filter) cuts the laser light in front of the monochromator; care has been taken in order to place the filter in a perpendicular position with respect to the incident laser light. Absorption spectra have been acquired by using a Perkin Elmer Instruments Lambda 900 spectrometer.

(D) SNOM Measurements Conditions

(i) Omicron Twin SNOM. We used two different modes for the near-field measurements: reflection and transmission-illumination. The first was for image processing while the second was for near-field spectroscopic measurements. We obtained all the results using the Omicron Twin SNOM shown in Figure 1(b). The same approach mechanism was adopted in both configurations. The only difference lies in the optical geometry of the system. The distance regulation system is of shear force type so that for each scanned region we obtain both topographic (phase and Z-height) and optical images in the constant distance mode. The average tip-sample distance is estimated to be in the order of few nanometers (the resolution in the Z direction being equal to 1 nm). The scan speed depends on the width of the selected image and the number of raster points per line. In average, the scan rate is 10 ms per raster point, with 350 points per line. Parameters have been chosen in order to have the scan speed with a lower limit that is duration of 4 s for a forward and backward scan line.

(ii) SNOM Tip Fabrication and Characterization. We fabricate our SNOM probes by applying the pulling and heating method [11] on standard single mode optical fibers (Thorlabs-SM 450) with 125 μm cladding diameter. An evaporator then covers them with a thin layer of Aluminum, having a thickness in the order of 80–100 nm. With this procedure, the tips have an aperture diameter that varies between 100 nm and 150 nm. Before and after each measurement, the state, shape, and transmission properties of each tip are controlled under a microscope and with an angular diagram setup. An angular diagram shows the spatial angular distribution of emitted rays from a probe's aperture when it is penetrated by a laser. The data collected permits one to deduce information about the shape and morphology of the tip. It also gives an average value of the aperture's dimensions. A typical angular diagram setup is shown in Figure 2(a).

The main setting consists of a photomultiplier tube which is fixed to a rotating arm that makes a half-circle trajectory in the XY plane around a SNOM tip. Laser light is injected in the tip, and the intensity of emitted light is recorded as a function of the rotating angle starting from $-90°$ till $90°$. The same step is repeated after rotating the SNOM tip around itself at angles ϕ of $60°$ and 120. Figure 2(b) shows a characteristic 3D far-field angular diagram for a well circularly shaped narrow tip, with no cracks or important protrusions at its end. We used tips with such typical diagrams in our measurements in order to avoid the occurrence of a SNOM image artifact, due to broken or blunt probes.

On the SNOM setup, the coarse positioning of the tip is done through a piezoelectric system implemented within the rotating arm. It moves the probe in the x, y, and z
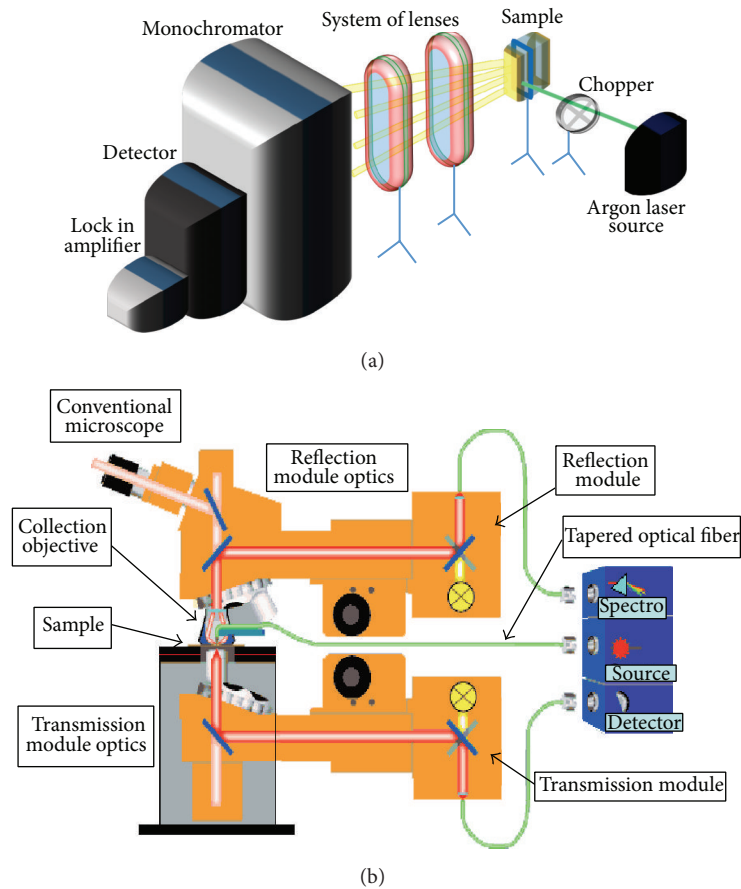
(a)

(b)

FIGURE 1: (a) Emission spectroscopy setup for nanoparticles in solution. The argon laser excites the sample, and the corresponding emitted light is collected by a system of lenses that directs it to a monochromator. The last is backed up by a detector and operational amplifier. The chopper modulates the laser light for amplification. (b) Near-Field Optical Microscope setup. A sample is placed on the sample holder and is excited by the laser via the tapered SNOM tip. Two modes for light collection are possible, transmission through the transmission module optics or reflection, through the collection objective. The corresponding spectrometer is for near-field spectroscopy and the SNOM light detector for near-field imaging of the collected signal.
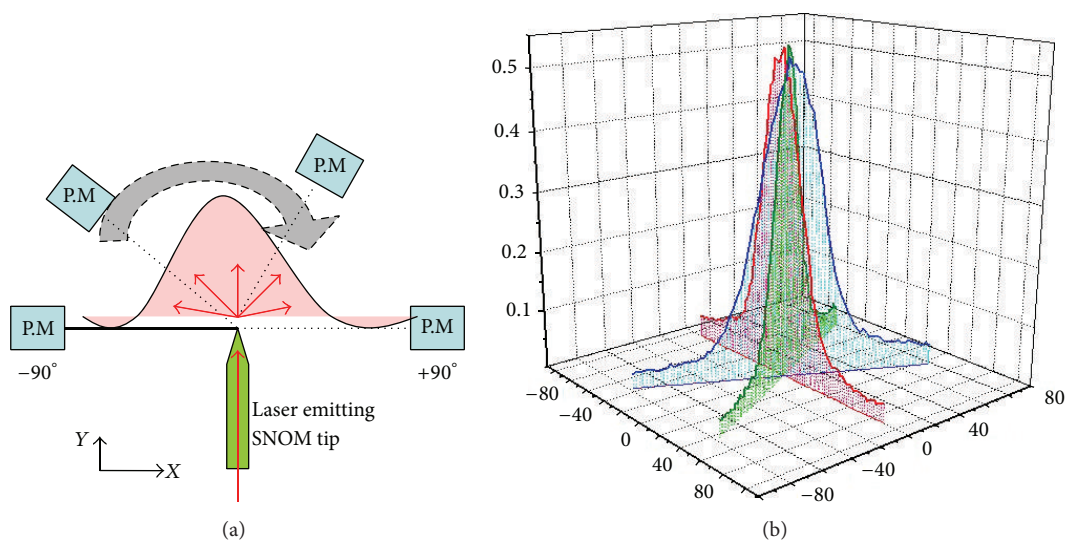

(a)

(b)

FIGURE 2: (a) Angular diagram setup. A laser light is injected into a SNOM tip and a photomultiplier tube collects the emitted light, scanning the region in front of the tip at $180°$. The SNOM tip is then rotated at different angles around itself and the scan repeated. (b) Typical angular diagram of a good quality SNOM tip. P.M refers to photomultiplier tube.
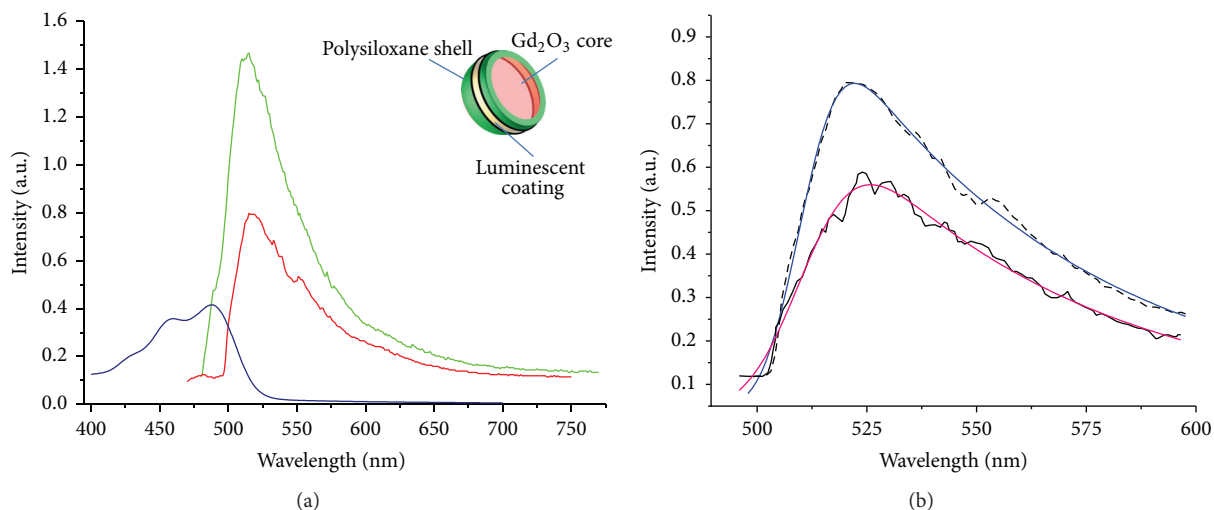
(a)

(b)

FIGURE 3: (a) Spectroscopic characterization of hybrid nanoparticles. The blue curve represents the absorption spectrum of the nanoparticles in water solution; the green curve is the corresponding emission spectrum at 488 nm excitation. The red curve is the emission spectrum of a dried drop of the same solution on a glass plate, at the same excitation wavelength (sample 1). *Inset*: hybrid nanoparticle configuration. The outer surface consists of a polysiloxane shell (green) covered with a luminescent coating that can be either Rhodamine or Fluorescein (yellow). The core is composed of a lanthanide oxide and gadolinium oxide (pink). (b) Comparison between near-field (dashed) and far-field (plain) emission spectra of hybrid nanoparticles, with corresponding blue and red curve fittings. The first has been obtained by using transmission mode SNOM. Intensity values have been normalized.

directions, with a maximum amplitude of $0.1 \times 0.1 \times 1 \, cm^3$. The piezoelectric table assures the control and sweeping of the samples position, with a resolution of $1 \times 1 \times 1 \, nm^3$.

The collection objective covering the tip is a combination of an ellipsoidal mirror and lenses. It collects about 80% of the emitted/scattered light, that is, making an angle of 53° and 85° [12] with respect to the probe axis.

(iii) SNOM Setup. During a SNOM measurement (Figure 1(b)), a laser beam is injected into the tapered SNOM tip through a lens coupling system, to excite the sample. The collection objective directs the emanating light toward a system of lenses, leading to the photomultiplier tube; two types of photomultiplier tubes are used, either a small Hamamatsu Photo sensor module (H7710-02 type) or a (C31034 series Burle type) photomultiplier tube when an increased sensitivity is needed. For fluorescence imaging, special notch filters are placed perpendicularly to the trajectory of the collected light. Exciting lasers are either a He-Ne (Melles-Griot) or a (Coherent Argon type) laser, depending on the desired wavelength. The power of the penetrating light is kept under a limit of about $1 \, \mu W$ so that the metallic layer covering the SNOM tip would not be harmed by an elevated laser power. Angular diagram measurements showed no melting effects with such parameters.

In transmission mode SNOM, the metalized tip is kept at a nanometric distance from the thin transparent sample and excites it. The transmitted light is directed via the transmission module optics toward either a spectrometer (Triax 180 Horiba Jobin Yvon type) or an imaging water cooled photomultiplier tube (R3310-02 Hamamatsu type).

2.1.2. Results

(A) Spectral Measurements. Figure 3(a) shows far-field absorption and emission spectra of the nanoparticles in solution; both are characteristic of FITC molecules [13]. Maximal peak absorption is at about 490 nm while emission is at 520 nm. In this configuration, the measured spectra represent the response of the system consisting of both solvent and nanoparticles. In order to be sure that no solvation effects interfered with the results, emission measurements were also conducted on sample 1; however, no important spectral impact was found, as shown in the same figure.

(B) Near-Field Studies

(i) Sample 1 Investigation. A typical near-field optical spectrum of sample 1 is shown in Figure 3(b). Far-field and near-field spectra are similar, and both peak at about 520 nm (scale has been normalized). The similarity between near- and far-field spectra has been obtained previously with different systems such as gold arrays [14], Si nanocrystals [15], or layered growth CdSe quantum dots samples [16]. It has been assigned in each case to different reasons such as spatial inhomogeneities, samples dimensions, or preparation conditions. In our case, the experiment took place at room temperature so that thermally activated processes lead to a broadening of the near-field spectrum. At the end of a measurement, highly topographic aggregations formed on the surface of sample 1. They were caused by the evaporation of the solvent in the air, as the nanoparticles solution drop laid on the glass substrate. During a SNOM scan, such formations hinder the shear force regulation of the SNOM probe. Consequently, sample 2 was

(a)

(b)

(A)   (B)   (C)
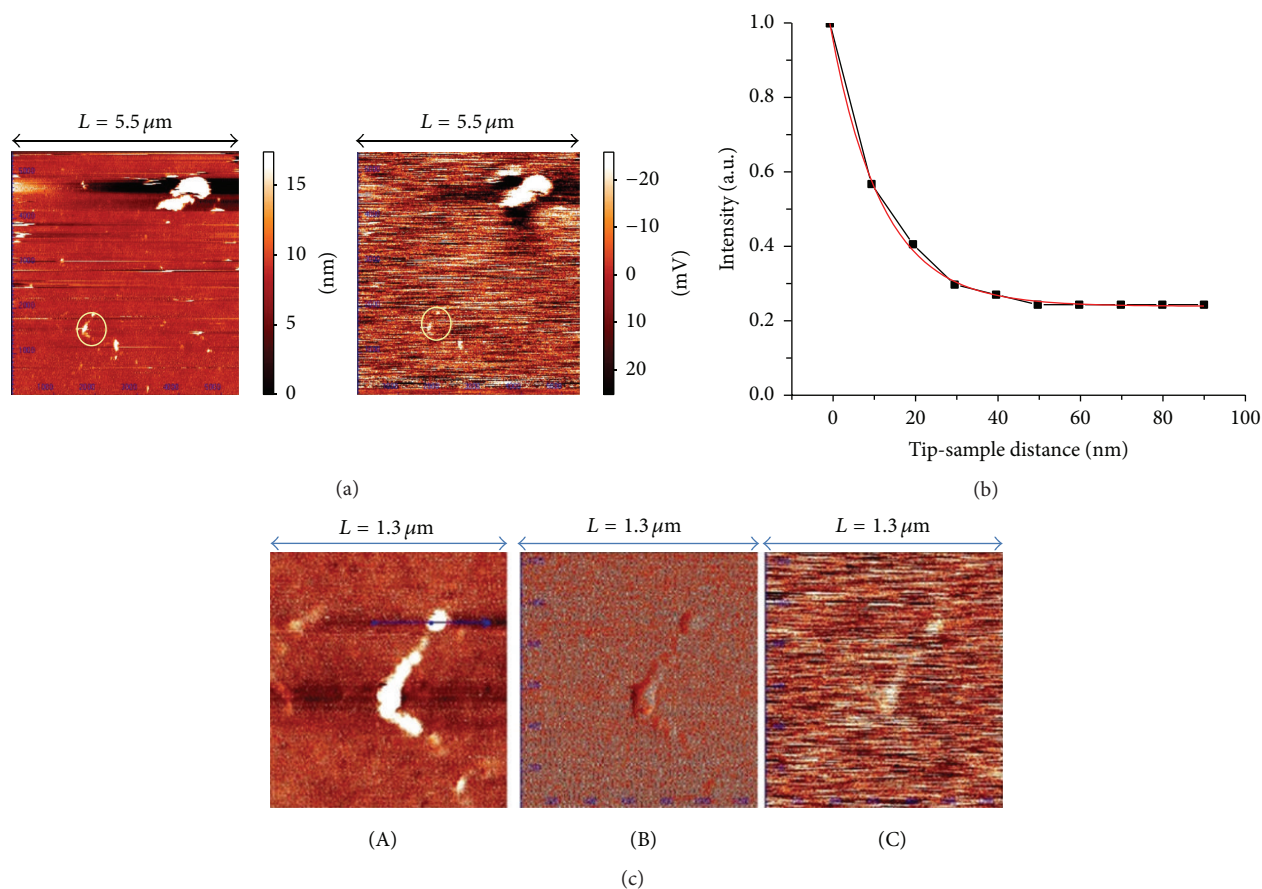
(c)

Figure 4: (a) Nanohybrid topographic (left) and optical (right) images. Aggregates of nanoparticles are represented by the randomly distributed white spots. The right-handed legend of the topographic image shows that the thickness of the formed clusters is about 20 nm, corresponding to one layer of nanohybrids. The optical image represents the scattered and fluorescent light emitted from the sample surface and aggregates. (b) Exponential decay curve (in black) of a hybrid nanoparticle aggregate in reflection mode SNOM. Corresponding exponential fitting (in red) is in accordance with decay data. (c) Z topographic (A), phase topographic (B), and an optical image (C) of zoomed part (in a circle) of (a). The blue arrow in the topographic image refers to the region for which profile line and resolution analysis studies are presented in the text (Sections 2.1.3(A) and 2.1.3(B)).

used for SNOM imaging. It is constituted of a single layer of hybrid nanoparticles repartitioned over the substrate surface, which can facilitate the scanning of the SNOM tip of the sample.

(ii) Sample 2 Investigation. Figure 4(a) shows 5.5 μm × 5.5 μm reflection mode near-field optical images of sample 2.

The left and right parts correspond, respectively, to topographic and optical images. The optical signal is a combination of both scattering and fluorescence light. The first comes from the scattering of the excitation laser while the last is emitted from the FITC molecules that are attached to the nanoparticles. The white dots represent aggregations of the deposited nanoparticles. The scale in the topographic image reveals that the aggregations height corresponds to the expected diameter of a nanoparticle (about 20 nm), implying that only one single layer of the nanoparticles has been deposited on the substrate.

Figure 4(c) shows, respectively, phase topographic, z topographic, and optical 1.3 μm × 1.3 μm images, obtained

by zooming into the lowest right part of Figure 4(a). Optical and topographic images resemble each other, even though the former presents a considerable background.

(iii) Exponential Decay Curve. We acquired exponential decay curves of the nanohybrids in order to make sure that no far-field signal had been collected. The SNOM tip had been initially fixed and the variation of the signal recorded as the tip approached the sample. The intensity data has been adjusted to account for the negative polarity of the detector. Figure 4(b) shows a near-field exponential decay curve, with the corresponding fit. The fit is perfectly exponential, with a Least Distance value of about 12 nm. Such a procedure has been repeated on many parts of the sample, and similar curves had been obtained, with a Least Distance value varying between 12 and 13 nm.

2.1.3. Discussion. In the previous section, we have presented constant distance near-field optical studies of nanohybrids. It appears possible to visualize such type of nanoparticles, by

Topographic image   Optical image

(i)

(ii)

(a)

Displacement (nm)   Displacement (nm)

d d $d + \Delta x$ $d - \Delta x$
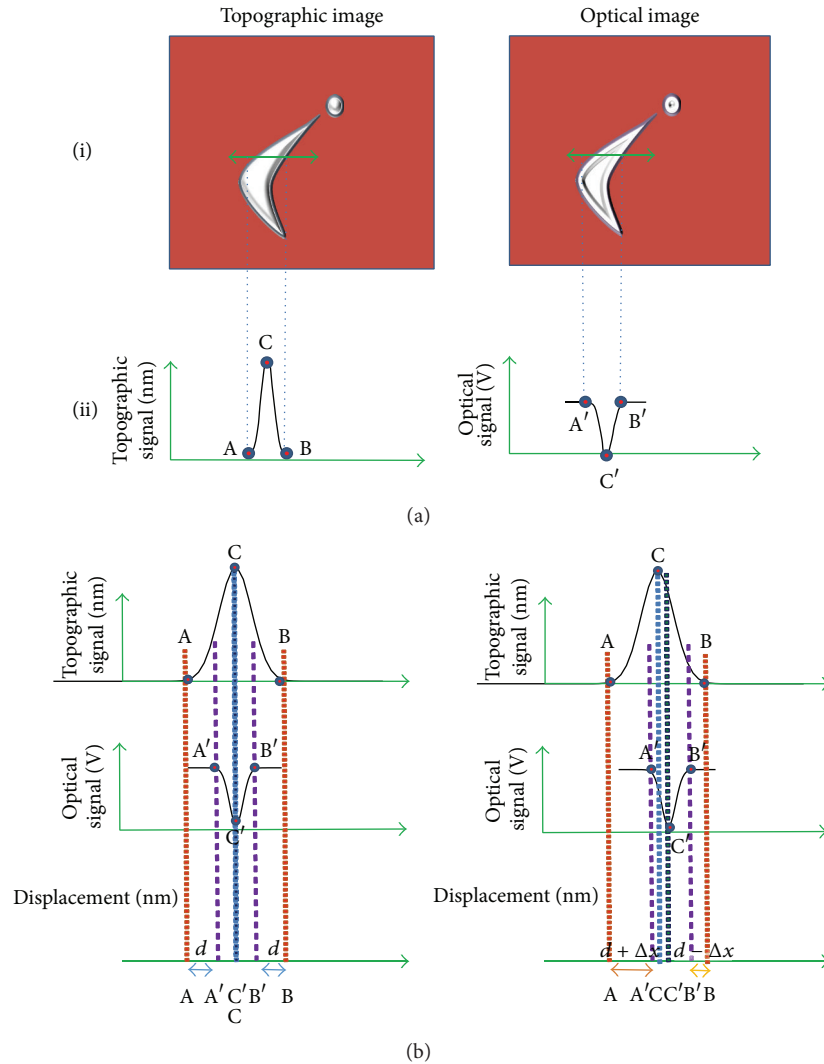
A A′ C′B′ B   A A′CC′B′ B
C

(b)

Figure 5: (a) Representation of scheme used for the study of topographic and optical profile line shift. The green arrow represents the region for which profile line analysis was done. Topographic and optical profile lines are delimited by points A, B, and A′, B′, respectively. Points C and C′ represent the corresponding peak signals. The optical signal is inverted downward since the detector we use has a negative polarity. (b) Comparison between topographic and optical profile lines with and without shift, as described in Section 2.1.3(B) in the text.

taking appropriate precautions pertaining to the nature of the sample and experimental conditions. We now demonstrate how one can verify the genuine nature of such images through an analysis of their resolution and positional shift.

(A) Resolution Discussion. Unlike conventional microscopy, the term "resolution" in Near-Field Optical Microscopy is still not fully defined [17]. In the second case, resolving power depends on parameters such as the probe-sample interaction, topography of the sample, scanning mode, size of the aperture, and polarization of the incident light [18, 19]. Being in the obligation to find a way to describe the discrimination between different elements in a SNOM image, groups in the scientific society used different definitions for resolution as follows:

(1) The width of the smallest discernible feature [11, 20].

(2) The Full Width at Half Maximum (FWHM) of a peak shaped feature [12, 20, 21].

(3) The width over which the signal drops from 90% of its maximum value to 10% [22–26]. This is called the "edge" or "rate resolution."

These definitions were used to evaluate the resolution of SNOM imaging for both fluorescence [20–22, 25] and scattering [11, 12, 17] cases. Figures 5(a) and 5(b) show a representation of topographic and optical profile lines that we used in order to calculate the resolution in our measurements.

For each image, an arrow is drawn, over a specific region (part (i)), and corresponding profile lines are plotted in part (ii). In (a-ii), topographic show the height variation of an object within the region under the blue arrow while optical profile lines represent the variation of the corresponding
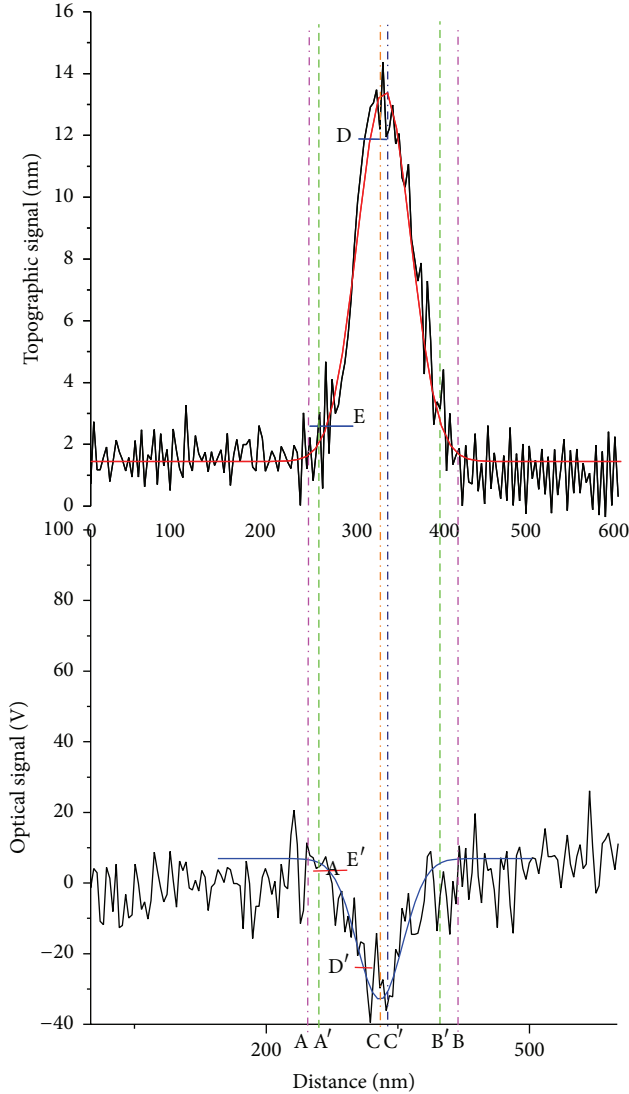
FIGURE 6: Profile lines of topographic and optical cross section of Figure 4(c), used for determining the rate resolution and optical/topographic shift. Marks D and E delimitate the edge resolution. Purple lines, cutting the distance axis at A and B delimitate the topographic profile line. Green lines delimitate the optical profile lines at A′ and B′. The shift between the two graphs is made obvious by the different lengths of AA′ and B′B. The two peak signals delimitated by C and C′ are also shifted one with respect to the other. As explained in the text, the shift value can be easily calculated by taking into consideration the difference between AA′ and BB′ and verifying with CC′.

optical signal. We will use similar profile lines for Figures 4(c) and 6.

The blue arrow in Figure 4(c) shows the region for which the profile lines are studied. The corresponding lines are fit with Gaussian functions and displayed in Figure 6; the blue marks set the points at which the vertical values of the fittings decrease from 90% to 10% of their highest value. They are denoted by D, E, and D′, E′ for, respectively, the topographic and optical profile lines. We calculate the edge resolution

by determining the horizontal distance that separates (D) from (E) and (D′) from (E′) (as in definition (3) above). The FWHM has been calculated after the fitting process.

Seemingly, the optical edge resolution (≈41 nm) is better than the topographic one (≈48 nm). Also, the respective FWHM follow the same pattern (FWHM$_{\text{topographic}} \approx$ 64 nm and FWHM$_{\text{optical}} \approx$ 51 nm). Attaining a different resolution in optical and topographic images is the sign of a genuinely pure optical SNOM image, free from z induced artefacts [1, 17, 22]. However, whether the optical resolution should be better or worse than the topographical one is still a point of debate [17, 19]. We assimilate the lack of resolution of SNOM topographic images to tip convolution at the steep edges of the studied structure.

We obtain images having average resolutions reaching values near 50 nm with a probe having a diameter of about 100 nm, in accordance with previous work in the literature [17]. In aperture SNOM, the finest resolvable structures are approximately equal to the aperture *radius* [1]. Such a resolution is assigned to the presence of a near-field scatterer in the vicinity of the aperture. These small particles (or mini tips) are formed on the aperture within the light pathway, acting as highly near-field scattering centers. It is consequently their size that is responsible for the high optical resolution.

(B) Image Artifacts. Many theoretical models have been established in order to describe SNOM tip-sample interaction and artifact formation. It was found that at least one of the following requirements had to be satisfied by a constant gap mode near-field image in order to be genuine [20, 21]:

(a) Topographic and near-field optical images are highly uncorrelated.

(b) Topographic and near-field optical images correlate but are shifted with respect to one another by a constant distance. In this case, optical and nonoptical zones do not coincide. The corresponding shift is caused by a displacement of the aperture with respect to the most protruding part of the tip, which is subject to shear forces [1, 27].

(c) The resolutions of near-field optics and shear force images are clearly different.

Due to the nature of our samples, we generally found a correlation between our topographic and optical SNOM images. Consequently, in order to verify their genuineness, we followed criteria (b) and (c). Figure 5(b) illustrates the method we used to verify criteria (b) for some given optical and topographic profile lines. In order to specify the shift between the images, we delimitate the borders of each profile line and mark the corresponding intersection with the x-axis. Points A and B represent the borders of the topographic image while A′ and B′ are for the optical one. Points C and C′ represent the topographic and optical signal peaks. We then compare between the positions of points A, B, and A′, B′. In the case where there is no shift (left image), the distance (d) between A, A′ and B, B′ is the same. If, however, the optical signal is shifted to the right by Δx, then the distance between A and A′ is ($d + \Delta x$) and that between B and B′ ($d - \Delta x$). By

$$L = 1.6\,\mu m \qquad\qquad L = 1.6\,\mu m \qquad\qquad L = 1.6\,\mu m$$

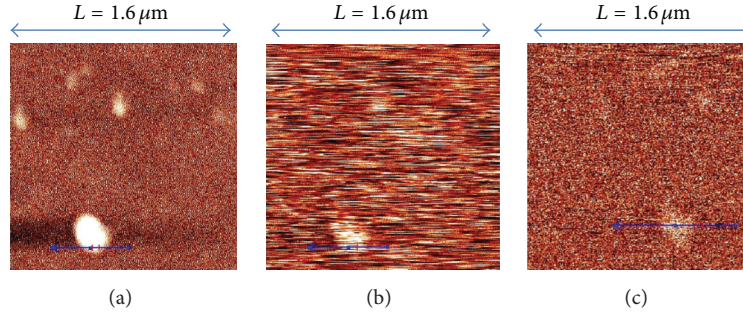(a)   (b)   (c)

FIGURE 7: (a) Topographic and (b) optical scattering and (c) fluorescence near-field images of hybrid aggregates. The blue arrow shows the region for which shift analysis was done. The difference between scattering and fluorescence imaging is clear, as much more noise is detected in the first case than in the second.

TABLE 1: Comparison table of topographic and optical images resolution for both edge and full-width half-maximum analysis methods.

	Edge resolution	FWHM resolution
Optical image	41 nm	51 nm
Topographic image	48 nm	64 nm

measuring $(d + \Delta x)$ and $(d - \Delta x)$, one can calculate the value of the shift Δx. The result can then be verified by comparing with the distance between C and C′.

Figure 6 shows the profile lines under the blue arrow in Figure 4(c). The procedure described above has been applied on the borders and peak and at a full-width half maximum (FWHM) of the signal. The corresponding shift was found to be about 8 nm. This is a reasonable value, taking into account the fact that the SNOM tips we use have an average radius of 50 nm.

Criterion (c) has already been proven fulfilled in Section 2.1.3(A). The different values obtained for both FWHM and edge resolution from the nanohybrid images are summarized in Table 1.

(C) Fluorescence/Scattering Imaging Genuineness. Figure 7 displays 1.6 μm × 1.6 μm topographic, scattering, and fluorescence optical images of hybrid nanoparticles aggregate.

The blue arrow shows the region for which the profile lines are studied. In the case of the scattering optical image, the profile line position was chosen in such a way as to show maximum contrast with the background. By following the same procedure as described in Section 2.1.3(B), one finds approximately the same 20 nm shift between scattering, topographic, and fluorescence images. This agrees with our experimental procedure, since the only intermediate step that we took between acquiring a fluorescence image and a scattering one is the placement of a notch filter in front of the detector, without lifting up of the SNOM tip from the surface.

In terms of resolution, the scattering optical images have an edge resolution of 80 nm and an FWHM equal to 90 nm; the corresponding topographic images have an edge resolution of 90 nm and an FWHM equal to 112 nm. Thus, in both cases, we are still encountering the situation where

the optical resolution is different from the topographic one. The fluorescence image is almost free from any background signal, contrary to the scattering one. In the last, the laser light scattered from the substrate, and nanoparticles fluorescence is collected by the detector. Consequently, the signal level differs for the two types of measurement (about 0.013 V for scattered light compared to 0.006 V for fluorescence).

In conclusion, we were able to prove in this section that the visualization of hybrid nanoparticles at high resolutions whether topographically (Z and phase topography) or optically (scattering or luminescence) is feasible by the use of Near-Field Optical Microscopy. The resolution which could be attained with our setup and the SNOM tips we used was found to reach values as small as 50 nm. Finally, as evidenced by the differently exposed methods, we have shown how to test the images we acquired for artifact free criteria. The conditions have been fulfilled in all the recorded images.

2.2. LSPR Imaging in the Near-Field. In the previous section, we have presented near-field optical images of nanoobjects that have similar topographic and optical features. Even though our procedures proved artifact-free image, we still wanted to make sure that the system we used guaranteed the repeatability of genuine images independently of the sample we studied. We consequently chose to investigate objects emitting through different processes than fluorophores emission. More precisely we were interested in studying objects that emitted light by Local Surface Plasmon Resonance (LSPR). LSPR takes place when a metallic object is placed in an electromagnetic field. The electric component of the last pushes the positively charged nuclei in one direction and the negatively charged electron cloud in the other [28]. As the electron cloud and nuclei are displaced one with respect to the other, a restoring Coulomb force arises between them, resulting in their oscillation. The constituted oscillating dipole emits in its turn an electromagnetic wave whose oscillation magnitude is at a maximum when a specific light frequency is used to illuminate the object. This results in maximum light emission or LSPR emission. The magnitude of emitted electric field can be calculated by applying Mie's theory [29] or quasistatic approximation calculation [30, 31], depending on the size of the studied object.
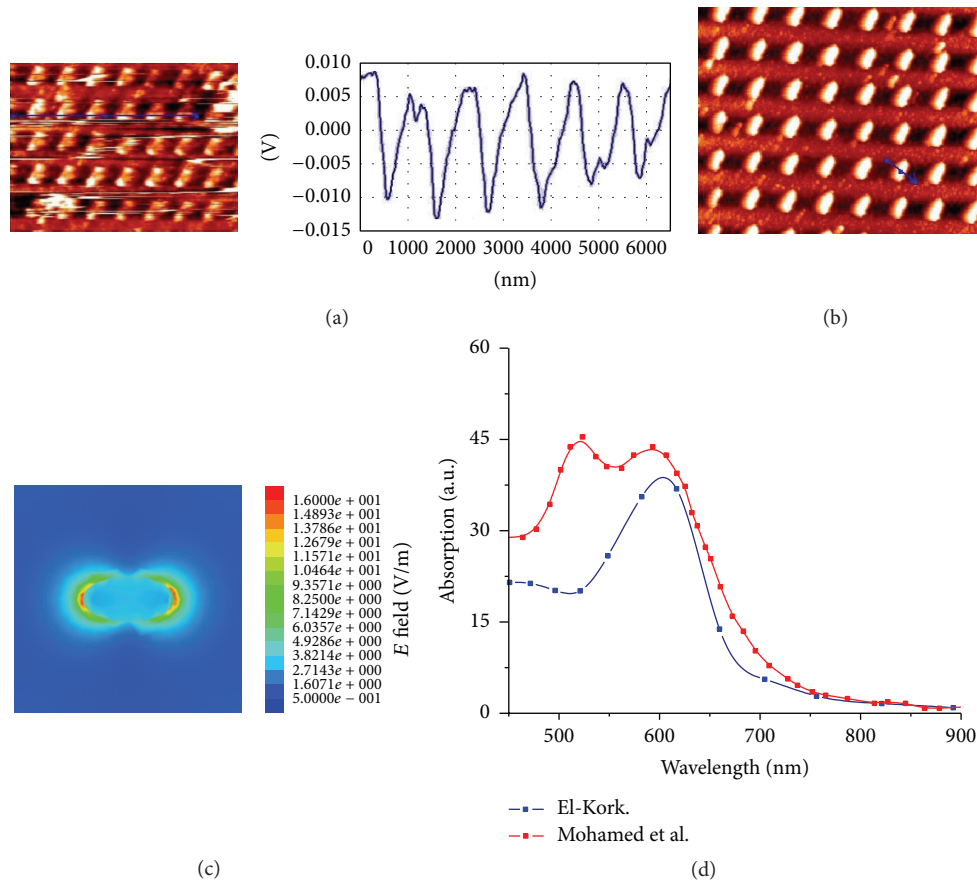
(a)

(b)

(c)

(d)

FIGURE 8: (a) left part: SNOM optical image of bare gold plots (sample A), excited at 633 nm. Two hot spots are clearly distinguishable on each plot. Right part: optical profile line of the region under the blue arrow. Signal peaks are separated according to the geometry of sample that is by 1 μm. (b) Near-field topographic image of the bare gold plots (sample A). The double hot spots pattern of (a) is replaced by well separated homogeneous solid ellipsoidal features. (c) Finite Element Simulation of the electric field on the surface of a gold nanoplot. The two red marks at the tips of the ellipsoid refer to the concentrated electric field or hot spots. (d) Simulated absorption spectrum of a gold nanoplot (blue curve); light is longitudinally polarized along the nanoplot major axis. The spectrum is compared with experiment, by Mohamed et al. (red curve). Both curves overlap along the longitudinal surface Plasmon resonance band.

In this section, we show near-field optical images of elliptical gold nanoplots that emit through LSPR. The shape of the plots has been chosen to be elliptical in order to visualize hot spots. Constant distance SNOM will be used as a tool for the genuine imaging of such nanoscopic photonic phenomena.

2.2.1. Experimental. The SNOM configuration used is the illumination reflection mode at room temperature. Electron Beam Lithography was used for the fabrication of gold spheroid disc arrays, each plot having a height of about 70 nm, and an equatorial diameter of 140 nm; the corresponding sample (A) is constituted of gold plots separated by 340 nm.

2.2.2. Results. Figure 8(a) is a near-field optical image obtained by illuminating sample A with a 633 nm linearly polarized laser and using a Notch filter to exclude the excitation laser.

Some regions of the optical image present signs of tip drifting (horizontal lines) or dust particles on the sample (large aggregate at the top part); still, one can perceive well the gold plot features. Each dot is characterized by two luminescent point sources (or "hot spots") that seem opposite to one another. Figure 8(b) is the corresponding topographic image. In this case, the double dot feature is replaced by an image of an ensemble of fully complete solid nanoplots.

Figure 8(c) shows a (2D) numerical simulation of the electric near-field distribution over an excited gold nanoplot. Figure 8(d) shows the corresponding scattering cross section spectrum. Both Figures 8(c) and 8(d) are based on Finite Element Method (FEM) calculations in the frequency domain, similar to that of Chau et al. [32, 33]; the Au permittivity data are also obtained from Johnson and Christy [34] and fitted to the Drude model, with corrections to include the particle size effect [35]. The spectrum peaks near 633 nm, making this wavelength suitable for LSPR excitation. Results have been compared with and are in accordance with previously obtained experimental results, with gold nanorods having the same aspect ratio [36]. The double shoulder in the simulation represents linear and longitudinal LSPR excitation. In our experimental case, we consider only the second shoulder as the excitation light is linearly polarized along the longitudinal axis of the gold plots.

2.2.3. Discussion. When nanoplots having an elliptical shape are placed in an external electromagnetic field, the corresponding electric field lines concentrate on their tips [37]. If applied at the right frequency, this electric field is responsible for the creation of LSPR at the surface of the nanorod. The intensity of the emitted light from the nanoplot is proportional to the square of its electric field. Figure 8(c) shows the simulation of the concentrated electric field at the end of a nanorod; it is also homologous to a plot of LSPR emission over the nanoplot surface. Maximal field intensities reach values as high as 16 V/m. Intrinsic luminescence in gold is attributed to a process which involves interband transition between s-p and d bands [38]. In the case of gold nanorods, El-Sayed et al. proved the coupling of the LSPR with an intrinsic sp-d intraband transition emission possible, causing its enhancement [36]. The corresponding emission spectra varied in emission wavelength and quantum yield, depending on the aspect ratio of each nanorod: as the length (or aspect ratio) of a nanorod increased, its emission wavelength shifted to lower energy and its quantum yield increased. Boyd et al. [39, 40] have shown that such results were based on a model in which the electronic excitations of very small spheroid metallic protrusion were found to be located at their apex.

The ellipsoidal nanoplots shown in Figure 8(a) are distinguished by characteristic luminescent spot at each end. These match well with the simulated spots in Figure 8(c). Figure 8(a) thus represent LSPR excitation in the form of the concentrated localized field on the plot tips. The illustrated dotted or "hot spot" features constitute a near-field optical image of the localized enhanced luminescence, on the apex of the nanoplots. Such "hot spots" have also been observed experimentally in the near-field on rough silver films [41]; their corresponding power and wavelength range depend closely on the shape of the nanoobjects on which they are located.

A comparison between Figures 8(a) and 8(b) certifies the importance of constant distance SNOM. In fact, in this case, topographic and optical images are highly uncorrelated due to the nature of the physical phenomena observed. One can clearly distinguish the difference between them: the former shows a double spotted feature while the latter is composed of whole solid shapes. Such dissimilarity and the correspondence between simulation and image is a proof that our images are artifact free. Also, as in the previous representation of gold nanohybrids on glass substrates, a comparison between optical and topographic images indicates a shift between them. This equally demonstrates the veracity of the system we use to acquire our images and the shift method used to ascertain the genuineness of a near-field optical image.

2.3. Near-Field Optical Microscopy of a Hybrid Biosensor. Biosensors are devices where a biological recognition element is built in and is a primary selectivity element [42]. A biosensor consists of a biological component that reacts with a target substance and a signal-generating component that detects the desired products or by-products. The product can be of chemical, biological, or biochemical nature and its detection can be associated with electrochemical [43], piezoelectric [44], or photometric mechanisms [45]. The later can be based on
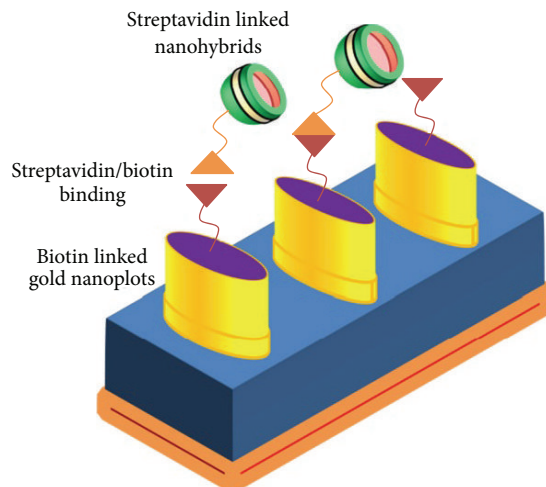

Figure 9: Nanohybrids biosensor principle: Biotin molecules (red shapes) are attached to gold nanoplots and hybrid nanoparticles are linked to Streptavidin proteins (orange shape). The strong covalent bond between Streptavidin and Biotin provides the stabilization of the nanohybrids on the gold nanoplots.

Local Surface Plasmon Resonance (LSPR). LSPR biosensors rely on the sensitivity of LSPR to a lot of parameters: the bandwidth, peak height, and position of an LSPR absorption maximum. These depend markedly on the size, size distribution, surface states, surface coverage, and surrounding of a given nanostructure [46–48].

The desired optical detection of nanoscopic analytes can be complex, given the sensitivity of available detection techniques. In order to overcome this problem, one may use Near-Field Optical Microscopy (SNOM), within the conditions of image genuineness.

In this section, we show how the use of SNOM can enhance hybrid biosensor performances and shed light on nanoscopic-sized detection. We use the bonding between two substances: Streptavidin and Biotin, to demonstrate the sensing mechanism in a sensitivity modulable gold plot biosensor.

2.3.1. Experimental

(A) Sample Preparation. Figure 9 is a representation of a nanohybrid biosensor.

Electron Beam Lithography was used for the fabrication of Au spheroid disc arrays, similar to sample A (in Section 2.2.2), except that the spacing between the Au spheroids is about 1400 nm.

The Biotin ligands were "glued" on the plots surface by immersing the last in a solution of trithiolated polypeptides modified with a Biotin molecule at their N-term end. After two hours, the plots were washed to remove all unbound molecules.

Biotin ligands bonded to Streptavidin molecules after immersing the substrate in a nanohybrids solution. The last contained Rhodamine (RBITC) and Streptavidin labeled nanohybrids, whose concentration was adjusted to obtain a functionalization ratio of one Streptavidin per particle.
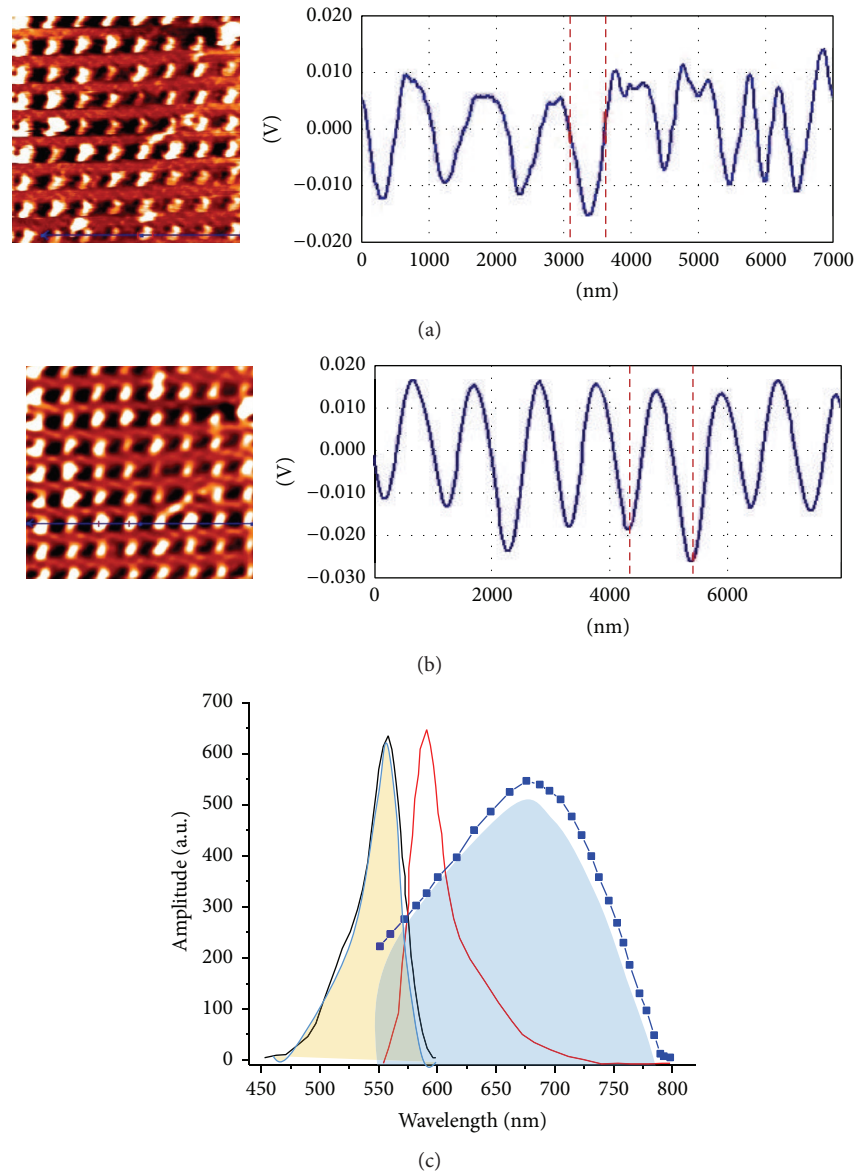
(a)

(b)

(c)

FIGURE 10: (a) left part: near-field optical image of gold plots covered by Streptavidin/Rhodamine molecules, excited at 633 nm. About 44% of the samples nanoplots emit light homogeneously, contrarily to the double spot feature in Figure 8(a). The dimensions of the image are slightly different from Figure 8(a). Right part: optical profile line of excited plots, within the region under the blue arrow. (b) Left part: near-field optical image of gold plots covered by Streptavidin/Rhodamine molecules, excited at 514 nm. About 83% of the samples nanoplots shine well. Right part: optical profile line of excited plots, within the region under the blue arrow. (c) Absorption (black) and emission spectra (red) of nanohybrids. Extinction spectrum of gold nanoplots is in blue. The area under the spectrum is shaded in light blue for more clarity.

(B) Investigation Procedure. The principle of the investigation consisted of determining if the biosensor was able to detect the presence of nanohybrids in the solution. In other words, we wanted to develop a nanoscaled method that detects the formation of a bond between the Streptavidin and Biotin molecules on the nanoplots. To do so, we compared the plots optical images before and after their immersion in the Streptavidin solution. Would there have been a disparity between the results, then binding would have taken place. The corresponding difference in luminescence would origin from the RBITC molecules that have been attached on the biosensor. We also illuminated the plots at different wavelengths, in order to see whether the biosensor is wavelength dependent and to determine the optimal conditions for nanohybrid detection. The SNOM configuration used is the illumination reflection mode. Three different excitation schemes have been adopted: first an illumination of the nonfunctionalized sample A by a 633 nm He-Ne laser, then the application of the same wavelength light, and finally a 514 nm argon laser on functionalized sample B.

2.3.2. Results. Figure 10(a) (left part) is obtained by exciting sample B with 633 nm. In this case, the double dot feature of Figure 8(a) is replaced by a quite homogeneously distributed

luminescence over some of the plots. Actually, about 44% of the samples nanoplots shine well, while the others emit partially; the right part of the figure shows a weak optical profile line for some selected plots.

Figure 10(b) (left part) represents sample B after its excitation with a 514 nm laser. This time, the homogeneously distributed luminescence is much more prominent than that in Figure 10(a), where 83% of the plots shine well and the emission much stronger, as shown by the corresponding high signal optical profile line (right part).

2.3.3. Discussion. The discrepancy between Figures 8(a) and 10(a) is a proof that the binding between Streptavidin and Biotin molecules has taken place. In other words, the nanoplots were able to "see" the nanohybrids in the solution. In fact, the homogeneous light distribution in Figure 10(a) represents the luminescence originating from the Streptavidin-Rhodamine molecules embedding the surface of the nanoplots. The absorption spectrum of Rhodamine in the visible range is composed of a band starting at 450 nm, peaking at about 540 nm and ending at 600 nm [49, 50]. As the excitation wavelength (633 nm) is outside this range, we assign the emission of light from Rhodamine to an indirect excitation process. The gold nanoplots absorb light at 633 nm [51] and emit a broad LSPR relaxation spectrum extending from 550 nm to 750 nm. This includes the margin within the 540–600 nm band for the excitation of Rhodamine as illustrated in Figure 10(c). Thus, the signal emanates first from the LSPR excitation and relaxation, and the emitted band then excites the Rhodamine, fluorescing at about 575 nm.

We can modify the sensing selectivity of the nanobiosensor by simply changing the excitation wavelength. We can control the strength of this signal-generating component since its response and that of the detected analytes are both wavelength dependent. Figure 10(b) presents an image of covered nanoplots with a much clearer contrast, a larger number of more homogeneously emitting nanoplots, and much better-defined features. In fact, 514 nm constitutes an appropriate wavelength for directly exciting Rhodamine and gold luminescence (through the sp-d interband transitions). Thus, in such a configuration, the excitation of the functionalized gold plots is due to both a direct excitation from the applied laser light at 514 nm and an indirect one coming from gold plots emission. These two phenomena lead to a maximized emission from Rhodamine, a higher quality and a much clearer contrast in Figure 10(b) compared to those of Figure 10(a). In other words, we are able to modulate the strength of the emitted signal or sensitivity of the biosensor by simply controlling the excitation wavelength.

3. Conclusion

We were able to show in this paper the importance of the topographic/optical shift method, in addition to the resolution difference method in SNOM images for the proof of image correctness. This method has been applied on nanohybrids fluorescing in solution and attached on gold plots. The veracity of the corresponding images has been demonstrated through LSPR emission, where simulations and experimental results corresponded well with each other. LSPR proved also as a valuable as a tool that permits the selective detection of specific analytes in the near-field, depending on the excitation wavelength. These results open the door for a safe, artifact free use of SNOM with biosensors, whether in constant height or constant distance mode.

Disclosure

Competing Interests

The authors declare that there are no competing interests regarding the publication of this paper.

Authors' Contributions

The paper was written through equal contributions of all authors. All authors have given approval to the final version of the paper.
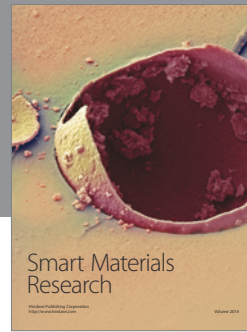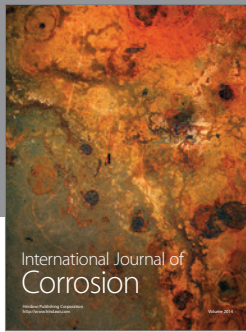
Acknowledgments

References

[1] B. Hecht, H. Bielefeldt, Y. Inouye, D. W. Pohl, and L. Novotny, "Facts and artifacts in near-field optical microscopy," *Journal of Applied Physics*, vol. 81, no. 6, pp. 2492–2498, 1997.

[2] G. Kaupp, A. Herrmann, and M. Haak, "Artifacts in Scanning Near-field Optical Microscopy (SNOM) due to deficient tips," *Journal of Physical Organic Chemistry*, vol. 12, no. 11, pp. 797–807, 1999.

[3] K. D. Weston, J. A. DeAro, and S. K. Buratto, "Near-field scanning optical microscopy in reflection: a study of far-field collection geometry effects," *Review of Scientific Instruments*, vol. 67, no. 8, pp. 2924–2929, 1996.

[4] P. Gómez-Romero and C. Sanchez, *Functional Hybrid Materials*, Wiley-VCH, New York, NY, USA, 2005.

[5] http://www.nano-h.com/.

[6] C. Louis, R. Bazzi, C. A. Marquette et al., "Nanosized hybrid particles with double luminescence for biological labeling," *Chemistry of Materials*, vol. 17, no. 7, pp. 1673–1682, 2005.

[7] C. Louis, S. Roux, C. Marquette et al., "Nanoparticules hybrides comprenant un coeur de Ln2O3 porteuses de ligands biologiques et leur procédé de fabrication," French Patent, no. 04.02115, 2004.

[8] R. M. van Hardeveld, P. L. J. Gunter, L. J. van IJzendoorn, W. Wieldraaijer, E. W. Kuipers, and J. W. Niemantsverdriet,

"Deposition of inorganic salts from solution on flat substrates by spin-coating: theory, quantification and application to model catalysts," *Applied Surface Science*, vol. 84, no. 4, pp. 339–346, 1995.

[9] A. Partridge, S. L. G. Toussaint, and C. F. J. Flipse, "An AFM investigation of the deposition of nanometer-sized rhodium and copper clusters by spin coating," *Applied Surface Science*, vol. 103, no. 2, pp. 127–140, 1996.

[10] Y.-K. Hong, H. Kim, G. Lee et al., "Controlled two-dimensional distribution of nanoparticles by spin-coating method," *Applied Physics Letters*, vol. 80, no. 5, pp. 844–846, 2002.

[11] B. Hecht, R. Zenobi, U. P. Wild et al., "Scanning near-field optical microscopy with aperture probes: fundamentals and applications," *The Journal of Chemical Physics*, vol. 112, no. 18, pp. 7761–7774, 2000.

[12] P. G. Gucciardi and M. Colocci, "Different contrast mechanisms induced by topography artifacts in near-field optical microscopy," *Applied Physics Letters*, vol. 79, no. 10, pp. 1543–1545, 2001.

[13] M. M. Martin, "Hydrogen bond effects on radiationless electronic transitions in xanthene dyes," *Chemical Physics Letters*, vol. 35, no. 1, pp. 105–111, 1975.

[14] L. Aigouy, F. X. Andréani, A. C. Boccara et al., "Near-field optical spectroscopy using an incoherent light source," *Applied Physics Letters*, vol. 76, no. 4, pp. 397–399, 2000.

[15] J. K. Trautman and J. J. Macklin, "Time-resolved spectroscopy of single molecules using near-field and far-field optics," *Chemical Physics*, vol. 205, no. 1-2, pp. 221–229, 1996.

[16] F. Flack, N. Samarth, V. Nikitin et al., "Near-field optical spectroscopy of localized excitons in strained CdSe quantum dots," *Physical Review B—Condensed Matter and Materials Physics*, vol. 54, no. 24, pp. R17312–R17315, 1996.

[17] M. Labardi, P. G. Gucciardi, M. Allegrini, and C. Pelosi, "Assessment of NSOM resolution on III-V semiconductor thin films," *Applied Physics A: Materials Science & Processing*, vol. 66, supplement 1, pp. S397–S402, 1998.

[18] J. Schöfer, M. J. Gregor, P. G. Blome, and R. G. Ulbrich, "Influence of aperture diameter on image contrast and resolution in scanning near-field optical microscopy," *Journal of Applied Physics*, vol. 81, no. 9, pp. 5871–5877, 1997.

[19] S. I. Bozhevolnyi, "Topographical artifacts and optical resolution in near-field optical microscopy," *Journal of the Optical Society of America B: Optical Physics*, vol. 14, no. 9, pp. 2254–2259, 1997.

[20] A. Dräbenstedt, J. Wrachtrup, and C. Von Borczyskowski, "A distance regulation scheme for scanning near-field optical microscopy," *Applied Physics Letters*, vol. 68, no. 24, pp. 3497–3499, 1996.

[21] R. Eckert, J. M. Freyland, H. Gersen et al., "Near-field fluorescence imaging with 32 nm resolution based on micro fabricated cantilevered probes," *Applied Physics Letters*, vol. 77, no. 23, pp. 3695–3697, 2000.

[22] J. M. Kim, T. Ohtani, and H. Muramatsu, "25 nm resolution single molecular fluorescence imaging by scanning near-field optical/atomic force microscopy," *Surface Science*, vol. 549, no. 3, pp. 273–280, 2004.

[23] V. Sandoghdar, S. Wegscheider, G. Krausch, and J. Mlynek, "Reflection scanning near-field optical microscopy with uncoated fiber tips: how good is the resolution really?" *Journal of Applied Physics*, vol. 81, no. 6, pp. 2499–2503, 1997.

[24] J. Koglin, U. C. Fischer, and H. Fuchs, "Material contrast in scanning near-field optical microscopy at 1–10 nm resolution," *Physical Review B*, vol. 55, no. 12, pp. 7977–7984, 1997.

[25] G. Y. Shanga, W. H. Qiaob, F. H. Leia, J. F. Angiboustb, M. Troyona, and M. Manfaitb, "Development of a shear force scanning near-field fluorescence microscope for biological applications," *Ultramicroscopy*, vol. 105, no. 1, pp. 324–329, 2005.

[26] L. T. Nieman, G. M. Krampert, and R. E. Martinez, "An apertureless near-field scanning optical microscope and its application to surface-enhanced Raman spectroscopy and multiphoton fluorescence imaging," *Review of Scientific Instruments*, vol. 72, article 1691, 2001.

[27] P. G. Gucciardi, M. Labardi, S. Gennai, F. Lazzeri, and M. Allegrini, "Versatile scanning near-field optical microscope for material science applications," *Review of Scientific Instruments*, vol. 68, no. 8, pp. 3088–3092, 1997.

[28] K. L. Kelly, E. Coronado, L. L. Zhao, and G. C. Schatz, "The optical properties of metal nanoparticles: the influence of size, shape, and dielectric environment," *The Journal of Physical Chemistry B*, vol. 107, no. 3, pp. 668–677, 2003.

[29] J. A. Lock and G. Gouesbet, "Generalized Lorenz-Mie theory and applications," *Journal of Quantitative Spectroscopy and Radiative Transfer*, vol. 110, no. 11, pp. 800–807, 2009.

[30] C. F. Bohren and D. R. Huffman, *Absorption and Scattering of Light by Small Particles*, John Wiley & Sons, New York, NY, USA, 2008.

[31] U. Kreibig and M. Vollmer, *Optical Properties of Metal Clusters*, Springer, Berlin, Germany, 1995.

[32] Y.-F. Chau, M. W. Chen, and D. P. Tsai, "Three-dimensional analysis of surface plasmon resonance modes on a gold nanorod," *Applied Optics*, vol. 48, no. 3, pp. 617–622, 2009.

[33] http://www.ansys.com/.

[34] P. B. Johnson and R. W. Christy, "Optical constants of the noble metals," *Physical Review B*, vol. 6, no. 12, pp. 4370–4379, 1972.

[35] S. Kawata, *Near-Field Optics and Surface Plasmon Polaritons*, vol. 81, Springer, Berlin, Germany, 2001.

[36] M. B. Mohamed, V. Volkov, S. Link, and M. A. El-Sayed, "The 'lightning' gold nanorods: fluorescence enhancement of over a million compared to the gold metal," *Chemical Physics Letters*, vol. 317, no. 6, pp. 517–523, 2000.

[37] D. Halliday, R. Resnick, and J. Y. Walker, *Fundamentals of Physics*, John Wiley & Sons, New York, NY, USA, 2008.

[38] A. Mooradian, "Photoluminescence of metals," *Physical Review Letters*, vol. 22, no. 5, pp. 185–187, 1969.

[39] G. T. Boyd, T. Rasing, J. R. R. Leite, and Y. R. Shen, "Local-field enhancement on rough surfaces of metals, semimetals, and semiconductors with the use of optical second-harmonic generation," *Physical Review B*, vol. 30, no. 2, pp. 519–526, 1984.

[40] G. T. Boyd, Z. H. Yu, and Y. R. Shen, "Photoinduced luminescence from the noble metals and its enhancement on roughened surfaces," *Physical Review B*, vol. 33, no. 12, pp. 7923–7936, 1986.

[41] V. A. Markel, V. M. Shalaev, P. Zhang et al., "Near-field optical spectroscopy of individual surface-plasmon modes in colloid clusters," *Physical Review B*, vol. 59, no. 16, pp. 10903–10909, 1999.

[42] P. T. Kissinger, "Biosensors-a perspective," *Biosensors and Bioelectronics*, vol. 20, no. 12, pp. 2512–2516, 2005.

[43] D. R. Thévenot, K. Toth, R. A. Durst, and G. S. Wilson, "Electrochemical biosensors. Recommended definitions and classification," *Biosensors and Bioelectronics*, vol. 16, no. 1-2, pp. 121–131, 2001.

[44] S. Tombelli, M. Minunni, and M. Mascini, "Piezoelectric biosensors: strategies for coupling nucleic acids to piezoelectric devices," *Methods*, vol. 37, no. 1, pp. 48–56, 2005.

[45] U. Narang, P. N. Prasad, F. V. Bright et al., "Glucose biosensor based on a sol-gel-derived platform," *Analytical Chemistry*, vol. 66, no. 19, pp. 3139–3144, 1994.

[46] E. Hutter and J. H. Fendler, "Exploitation of localized surface plasmon resonance," *Advanced Materials*, vol. 16, no. 19, pp. 1685–1706, 2004.

[47] T.-J. Lin, K.-T. Huang, and C.-Y. Liu, "Determination of organophosphorous pesticides by a novel biosensor based on localized surface plasmon resonance," *Biosensors and Bioelectronics*, vol. 22, no. 4, pp. 513–518, 2006.

[48] T.-J. Wang and W.-S. Lin, "Electro-optically modulated localized surface plasmon resonance biosensors with gold nanoparticles," *Applied Physics Letters*, vol. 89, no. 17, Article ID 173903, pp. 1–3, 2006.

[49] K. Kim, Y. M. Lee, J. W. Lee, and K. S. Shin, "Metal-enhanced fluorescence of rhodamine B isothiocyanate from micrometer-sized silver powders," *Langmuir*, vol. 25, no. 5, pp. 2641–2645, 2009.

[50] A.-C. Faure, C. Hoffmann, R. Bazzi et al., "Functionalization of luminescent aminated particles for facile bioconjugation," *ACS Nano*, vol. 2, no. 11, pp. 2273–2282, 2008.

[51] G. Barbillon, A. C. Faure, N. El Kork et al., "How nanoparticles encapsulating fluorophores allow a double detection of biomolecules by localized surface plasmon resonance and luminescence," *Nanotechnology*, vol. 19, no. 3, Article ID 035705, 2008.

Journal of
Nanotechnology

International Journal of
Corrosion

International Journal of
Polymer Science

**Smart Materials
Research**

Journal of
Composites

**BioMed
Research International**

Journal of
Metallurgy

Journal of
Materials

Journal of
Nanoparticles

Advances in
Materials Science and Engineering

Scientifica

Journal of
Nanomaterials

**The Scientific
World Journal**

International Journal of
Biomaterials

Journal of
Nanoscience

Journal of
Coatings

Journal of
Crystallography

Journal of
Ceramics

Journal of
Textiles

Hindawi

Submit your manuscripts at
http://www.hindawi.com